PHYSICAL REVIEW A **111**, 012610 (2025)

Probing electron-photon entanglement using a quantum eraser

Jan-Wilke Henke, Hao Jeng, and Claus Ropers*
Max Planck Institute for Multidisciplinary Sciences, 37077 Göttingen, Germany
and 4th Physical Institute, University of Göttingen, 37077 Göttingen, Germany

(Received 18 April 2024; accepted 18 December 2024; published 9 January 2025)

We propose a tangible experimental scheme for demonstrating quantum entanglement between swift electrons and light, relying on coherent cathodoluminescence for photon generation in a transmission electron microscope, and a quantum eraser setup for formation and verification of entanglement. The entanglement of free electrons with light is key to developing free-electron quantum optics and its potential applications such as quantum sensing, novel photonic and electron state generation, and entanglement between free electrons.

DOI: 10.1103/PhysRevA.111.012610

I. INTRODUCTION

Entanglement between different subsystems or degrees of freedom is a defining hallmark of quantum science and underpins unique applications in emerging quantum technologies such as quantum computation [1,2], communication [3–5], and sensing [6,7]. While entanglement can occur naturally by simply letting two quantum systems interact, it is also notoriously fragile and difficult to observe because the quantum correlations are easily overwhelmed by decoherence.

The quantum eraser provides a particularly striking and conceptually instructive demonstration of quantum entanglement [8]. In this scheme, the introduction of a marker particle carrying which-path information eliminates single-particle interference in interferometric setups. The removal of this which-path information on the entangled marker, however, allows for the recovery of the multipath interference. With the addition of suitable inseparability criteria [9–13], one could verify if the two parties of the system exist in a state of entanglement. Initially proposed as a gedanken experiment, the quantum eraser has been demonstrated with photons [14–18], atoms [19], electrical circuits [20], and phonons [21].

Perhaps surprisingly, the possibility of entangling fast electrons, used in electron microscopy for research on nanoscale structures and dynamics [22–24], has only recently begun to attract attention [25–28], despite their exceptional controllability and favorable coherence properties. Spontaneous inelastic scattering of electrons is routinely employed in the study of optical excitations [29], and quantum optics has entered this field in the form of photon correlation spectroscopy [30–33]. The stimulated inelastic interaction with optical near fields is quantum coherent [34,35] and has enabled optical field characterization [36–38], reconstruction of the free-electron quantum state [39], and free-electron homodyne detection [40]. Numerous applications harnessing the quantum nature of this inelastic electron-light scattering and the resulting correlations have been suggested, including probing of quantum optical excitations [41,42], correlation-enhanced imaging [43,44], improved measurement sensitivity in interaction-free measurements [45–48], and the generation of quantum states of light [49–52]. However, while the underlying interactions are expected to induce electron-photon entanglement [28,43], facilitate electron-electron entanglement [26], or even mediate photon-photon entanglement [53], studies thus far have fallen short of direct proof.

The objective of this paper is to describe experimental scenarios for demonstrating the entanglement of free electrons and light. For illustrative purposes, we first consider the suppression and subsequent recovery of single-electron interference resulting from quantum correlations in a quantum eraser scenario. Specifically, we introduce a double-slit geometry producing entanglement between photon degrees of freedom and the electron position. Addressing experimental implementations, we propose dual-point probes as used in scanning transmission electron microscopy (STEM) holography and coincidence measurements to generate optical excitations at designed photonic structures to form an entangled bipartite state and perform characterizing measurements. Finally, we relate the measurements in this quantum eraser scenario to entanglement tests such as quantum state tomography of the electron-photon system and discuss a transfer also to free-electron–electron entanglement.

II. CONCEPT OF QUANTUM ERASURE

The basic idea of a quantum eraser relies on single-particle interference observable behind a double-slit structure. When introducing a marker, entangled with the interfering particle and providing which-path information, the interference disappears but can be recovered using a basis change on the marker and coincidence detection [8]. These concepts can

---

*Contact author: claus.ropers@mpinat.mpg.de

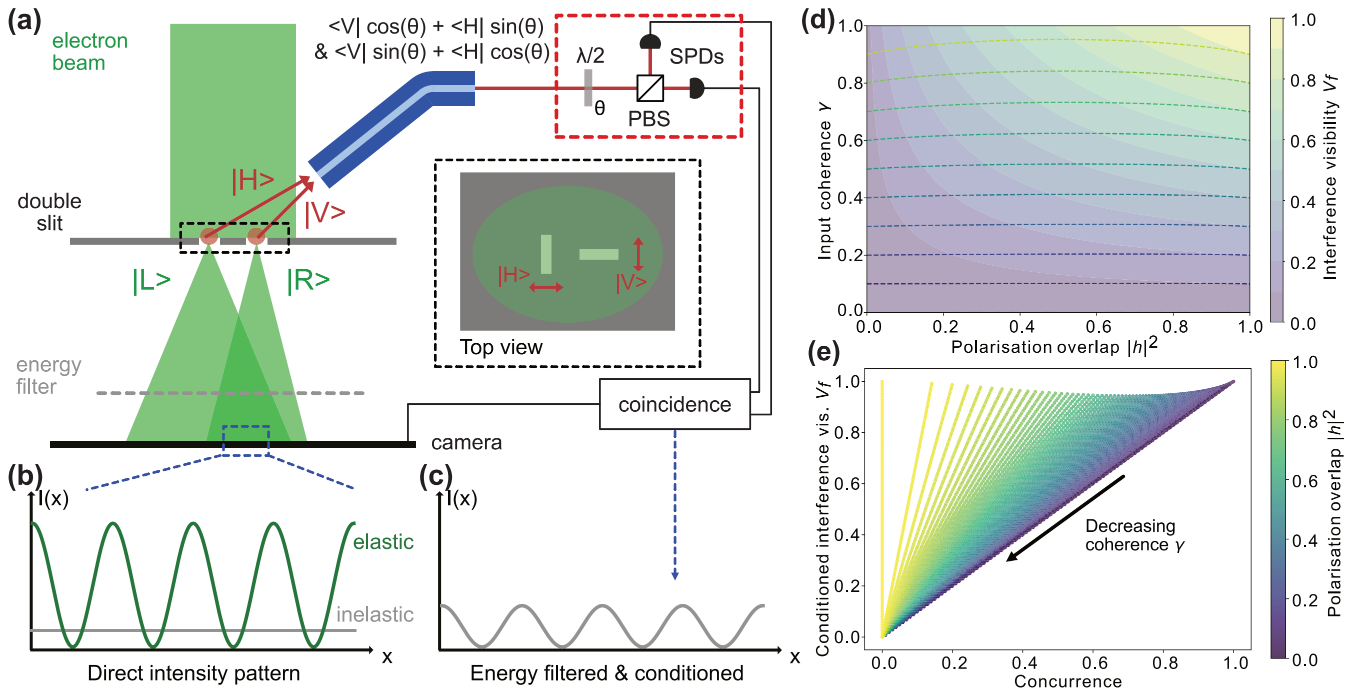

FIG. 1. Quantum eraser experiment with free electrons. (a) An electron beam illuminates a double-slit structure. Electrons (green) passing through the left (quantum state $|L\rangle$) and right ($|R\rangle$) slit generate identical photons (red) of orthogonal polarizations $|V\rangle$ and $|H\rangle$ as highlighted in the inset. These marker photons are collected with a fiber (blue), passed through a half waveplate ($\lambda/2$) of variable orientation θ and a polarizing beam splitter (PBS) before detection on single-photon detectors (SPDs), thus realizing projective measurements on superposition of $|H\rangle$ and $|V\rangle$ (dashed red box). The electrons are energy filtered for one-photon loss (gray dashed line) and detected on a camera, enabling coincidence detection of electrons and photons. (b) Direct intensity distribution behind the energy filter exhibiting interference fringes when no marker photon is generated (green) and no interference (gray) when orthogonal marker photons are generated. (c) Interference pattern recovered from coincidences of energy-filtered electrons and photons after local operations with the wave plate. (d) Visibility V_f of the interference fringes depending on the input coherence γ and the overlap of the marker photons $|h|^2$ in the direct (colormap and solid lines) and conditioned intensity distribution (dashed lines). (e) Interference fringe visibility V_f in the recovered distribution versus the concurrence C of the electron-photon state for different polarization overlap $|h|^2$ (color coded) and input coherence (direction of decreasing input coherence γ indicated by a black arrow).

be applied to experiments with free electrons, as illustrated in Fig. 1(a).

When a fully coherent electron beam homogeneously illuminates a double-slit structure, interference causes an oscillation in the intensity distribution in the far field [54–56]. The intensity pattern, given by $I(x) \approx I_0(x)\{1 + \cos[\phi(x)]\}$ with the diffraction pattern of a single slit $I_0(x)$ and the phase difference between the propagation pathways $\phi(x)$ (see Appendix A for details), can be detected using a camera as shown in Fig. 1(b).

Suppose that electrons passing through the slits generate distinguishable photons, e.g., in different spatial modes or of orthogonal polarization. For simplicity, assume that transmission through the left (right) slit gives horizontally (vertically) polarized photons, denoted by $|H\rangle$ and $|V\rangle$, respectively. This results in an entangled electron-photon state

$$|\psi\rangle = \frac{1}{\sqrt{2}}(|L, H\rangle + |R, V\rangle) \tag{1}$$

behind the slit with the generated photons carrying which-path information about the electron, eliminating the electron interference pattern [gray line in Fig. 1(b)]. An electron energy filter [dashed gray line in Fig. 1(a)] selects the fraction of electrons that produced a marker photon and lost the corresponding energy.

The interference pattern can however be restored with a photon state basis change and a projective measurement. To this end, the marker photons are collected via an optical single-mode fiber and passed through a half waveplate as well as a polarizing beam splitter [red box in Fig. 1(a)]. The waveplate effectively erases the which-path information by mixing the polarization states rendering the single-photon detectors (SPDs) placed behind a polarizing beam splitter (PBS) unable to distinguish the electron paths. The detection of electrons in coincidence with a photon on one of the SPDs will result in a recovered interference pattern as shown in Fig. 1(c). Similarly, coincidences between electrons and the other SPD will yield an interference pattern that is phase shifted by π, making coincidence detection with a single SPD necessary to retrieve the interference. In contrast to photonic realizations of the quantum eraser, based on pairs of photons entangled in polarization [15,16] or momentum [14,57], the electron position in the plane of the double slit is entangled with the polarization of a photon generated by the electron. Measurements of the electron-diffraction pattern then correspond to the (conditioned) polarization or momentum state analysis in photonic quantum erasers.

III. EXPERIMENTAL CONSIDERATIONS

Under realistic experimental conditions imperfections in the marker-photon-generation process, the electron-beam preparation or the optical setup will hamper the elimination and coincidence-based recovery of the interference pattern. A deviation from perfectly orthogonal marker-photon states, for example, the case of electrons passing through the right slit generating a photon in a superposition of polarizations $h|H\rangle + v|V\rangle$ will impact the observed intensity patterns. The unconditioned intensity distribution I_u of electrons that generated a photon then reads (see Appendix A)

$$I_u(x) = I_0(x) + \mathrm{Re}(h)I_0(x)\cos[\phi(x)],$$

while the recovered conditioned interference pattern I_c, formed by electrons coincident with a which-path erased photon on one of the SPDs, becomes

$$I_c(x) = [1 + \mathrm{Re}(h^*v)]I_0(x) + \mathrm{Re}(h + v)I_0(x)\cos[\phi(x)].$$

Notably, I_u exhibits oscillations depending on the overlap $|h|^2$ of the marker-photon states. A larger overlap reduces the which-path information about the electron and is directly linked to a reduced degree of electron-photon entanglement. This can be quantified via the concurrence C [10,58], an entanglement measure for a two-qubit system related to the entanglement of formation [9]. It takes on values $0 \leqslant C \leqslant 1$, with the extremes given by separable and maximally entangled states, respectively, and can be expressed as $C = |h|$ for our scenario with a pure state.

Any principal distinguishability of the marker photons in other degrees of freedom, such as the wavelength, will reduce the visibility of the interference fringes $V_f = (I_{\max} - I_{\min})/(I_{\max} + I_{\min})$ due to the reduced overlap in the partial trace. Careful design of both the sample and the optical setup is therefore paramount to avoid this in the generation and propagation of the photons.

Similar care needs to be taken in the preparation of the electron beam, as limited spatial coherence $\gamma < 1$ will suppress the off-diagonal elements of the bipartite state's density matrix and thus impose an upper bound on the concurrence. This is accompanied by a reduction of visibility in both the unconditioned and recovered interference patterns.

These findings are summarized in Figs. 1(d) and 1(e), with Fig. 1(d) showing the dependence of the fringe visibility V_f in the direct pattern (contours and solid) and reconstructed conditioned pattern (dashed lines) on the polarization state overlap $|h|^2$ and input beam coherence γ. The former increases with the overlap $|h|^2$ and is bounded by the degree of coherence, while the latter exhibits only small variations. When comparing the recovered interference fringe visibility V_f with the concurrence C of the electron-photon state within our simple model [see Fig. 1(e)], we find an almost perfect linear relation for small polarization overlap $|h|^2 < 0.1$. In these cases, quantum erasure, signaled by the recovery of interference fringe visibility after conditioning, can be considered an indicator of electron-photon entanglement. To achieve a concurrence of $C \geqslant 0.3$ and verify electron-photon entanglement by this comparison of unconditioned and conditioned intensity patterns, we estimate requirements for the parameters of $|h|^2 < 0.25$ and $\gamma \geqslant 0.35$. These are well within reach of current experimental setups both concerning the generation of polarized photons [59,60] and electron coherence [61–64] (for additional information, see Appendix B).

IV. POSSIBLE EXPERIMENTAL REALISATIONS

An experimental realization of free-electron–photon quantum erasure, accordingly, requires, first, a highly coherent and controllable electron beam to illuminate a double-slit-type structure; second, efficient generation of distinct marker photons carrying the electron which-path information in a single degree of freedom; and third, the capability to collect marker photons, manipulate their quantum state, and perform projective measurements in coincidence with energy-filtered electron detection in the diffraction pattern.

Transmission electron microscopes (TEMs), particularly those with field-emission electron sources, provide a well-controlled and coherent electron beam, enabling, e.g., electron holography [62,63]. Splitting the electron beam, as illustrated in Fig. 2(a), rather than using a transmissive double-slit structure slightly relaxes the coherence requirements and significantly increases the effective electron current. The splitting can, for example, be achieved by deflection using an electrostatic biprism [56,62] or diffraction from a holographic phase or amplitude plate in the TEM's condenser system [65,66]. Amplitude plates, schematically depicted in Fig. 2(b), require careful design and fabrication to ensure low losses and a deflection of electrons mainly into the first diffraction order, whereas a biprism [cf. Fig. 2(c)] allows tunable separation of beams but demands higher beam coherence as different sections of the beam need to interfere. In both cases, the beams must be overlapped below the sample to observe interference [cf. Fig. 2(a)], through either the imaging lenses or additional beam-splitting elements in a Mach-Zehnder interferometer scheme [67].

Distinguishable marker photons for the two electron pathways can be generated via different coherent parametric processes [29,68], including inelastic electron-light scattering, Smith-Purcell radiation, or transition radiation. Two possible geometries allowing for the entanglement of the electron position with different photonic degrees of freedom are presented in Figs. 2(d) and 2(e).

Our first suggestion [Fig. 2(d)] involves polarized photon generation at a specifically shaped metallic structure placed in front of a single optical fiber. Fast electrons impinging on a metallic surface generate transition radiation due to the annihilation of the image charge in the material, leading to the emission of polarized electromagnetic radiation [29]. Tailoring the boundary properties, electrons hitting the metallic plateau at different positions relative to the fiber core will generate different photon polarizations. At typical TEM energies, the photon-generation efficiencies are on the order of 10^{-3} and the emission is broadband [29], rendering the nonorthogonality of marker photons the main concern for the recovered electron fringe visibility. The required manipulation of the photon state and erasure of which-path information can be implemented using waveplates, a PBS, and SPDs as indicated in Figs. 1(a) and 2(d).

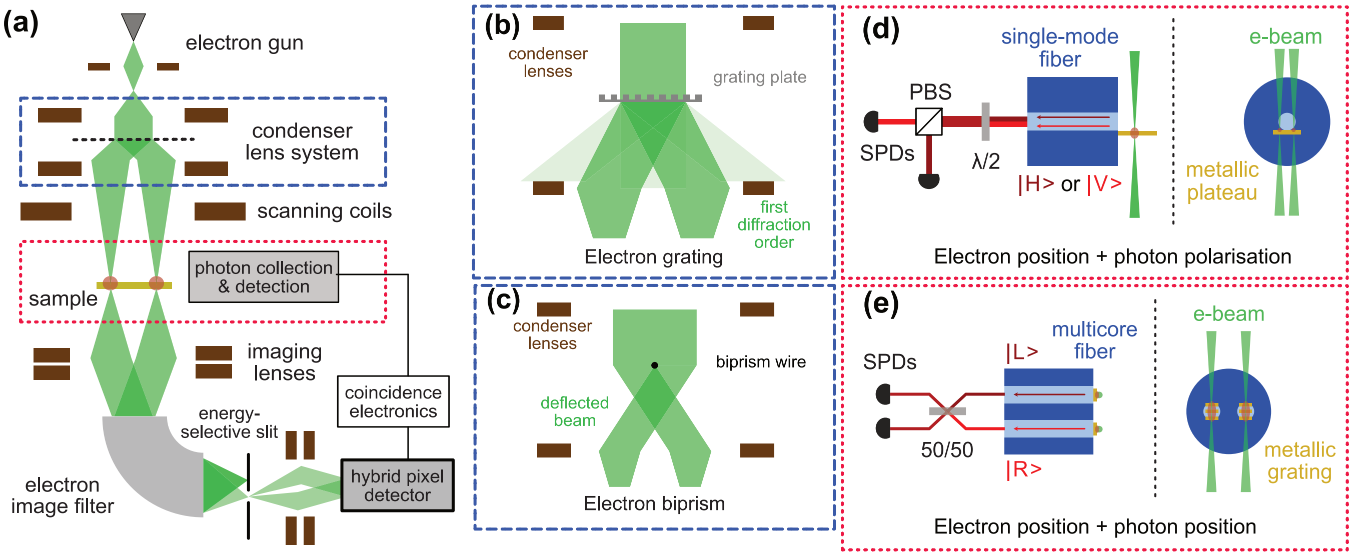

FIG. 2. Possible implementations of a quantum eraser experiment. (a) Key elements of a free-electron quantum eraser are electron-beam splitting, efficient marker-photon generation and collection, and coincidence detection. Splitting the electron beam in the condenser system [blue box, details in (b) and (c)], two focused electron probes are formed at the sample. There, distinguishable marker photons are generated and collected for further processing [red box, details in (d) and (e)]. Below the sample, an imaging filter selects electrons that generated a marker photon before recombining the beams to give an interference pattern on a hybrid-pixel detector that enables coincidence detection of electrons and photons. (b) The splitting of the electron beam can be achieved, for example, by a grating plate causing diffraction of the electron beam. (c) Alternatively, an electron biprism consisting of a thin biased wire deflecting parts of the input beams in different directions can be used. (d) The generation of polarized photons ($|H\rangle$ or $|V\rangle$), e.g., in transition radiation, at a specifically designed structure placed in front of an optical fiber allows for marker-photon generation and collection. Manipulation of the which-path information is then achieved by a waveplate ($\lambda/2$) and a polarizing beam splitter in front of the single-photon detectors. (e) Alternatively, marker photons can be generated via Smith-Purcell radiation coupled to different fiber cores, yielding photons in the states $|L\rangle$ or $|R\rangle$. An erasure of the which-path information can then be implemented using a balanced beam splitter (50:50) before the SPDs.

Alternatively, one could achieve entanglement of the electron path and the generated photon position at the end face of a multicore fiber [cf. Fig. 2(e)] or the photon propagation direction at an optical waveguide. In the former case, grating structures imprinted on metal-coated fiber end faces facilitate photon generation in the different fiber cores $|L\rangle$ or $|R\rangle$ via the Smith-Purcell effect [69,70]. The electrons' evanescent field is diffracted into the fiber with the emission wavelength and direction determined by the grating parameters and the electron velocity [29,68]. The latter scenario uses inelastic scattering of free electrons at the vacuum field of a well-defined resonator mode [26,71], with phase-matched interactions shown to enable the generation of correlated electron-cavity photon pairs in integrated photonic circuits [43]. In both cases, erasure of the electron which-path information can be achieved by a balanced beam splitter mixing the two photon pathways. Despite higher potential photon-generation efficiencies, these scenarios require larger electron-beam separations and precise sample design to ensure required marker-photon properties, thereby posing additional experimental challenges. Other experimental geometries, e.g., based on parabolic mirrors for free-space photon collection [30,44], and harnessing different coherent cathodoluminescence processes are also possible.

An energy-filtering electron imaging spectrometer, illustrated at the bottom of Fig. 2(a), can select electrons that lost energy corresponding to that of a generated photon [72,73]. This filtering suppresses the majority of unscattered electrons that would otherwise yield an elastic interference pattern [cf. Fig. 1(b)]. In combination with a hybrid-pixel electron detector, a time-, energy-, and position-resolved detection of the electrons is possible, enabling the required coincidence-based measurements in conjunction with the single-photon detection [43,44]. This coincidence detection of electrons in the energy-loss window and photons, crucial for the recovery of the interference pattern, additionally allows for improving the signal-to-noise ratio by removing accidental counts of electrons that did not generate a photon, i.e., were scattered in different inelastic channels or are in the tail of the incident electron energy distribution.

V. TESTS FOR INSEPARABILITY

Measurements performed with the quantum eraser setup can also more generally be used to determine whether the electron-light system is entangled. Let us denote the Pauli matrices by σ_x, σ_y, and σ_z as usual and associate the photon and electron states $\{|H\rangle, |V\rangle\}$ and $\{|L\rangle, |R\rangle\}$ with the eigenvectors of σ_z. Then the fidelity of any given state with respect to the Bell state in Eq. (1) can be expressed as $F = (1 + \langle\sigma_x \otimes \sigma_x\rangle - \langle\sigma_y \otimes \sigma_y\rangle + \langle\sigma_z \otimes \sigma_z\rangle)/4$, and a value greater than $\frac{1}{2}$ provides a sufficient condition for entanglement [10]. In our quantum eraser setup, these correlation functions can be obtained by first measuring the photon in the respective basis, i.e., σ_x, σ_y, or σ_z, and then summing up the visibilities of the electron interference fringes observed when conditioning on each of the photon states in that basis. Not all situations where interference fringes are recovered correspond to entanglement, however, just those where the visibilities are large enough that the inequality above is satisfied.

Interestingly, tomographic reconstruction of the two-qubit electron-photon density matrix is also possible, since all independent combinations of Pauli measurements can be implemented (see Appendix C). Consequently, it is straightforward to determine whether the state is entangled by using entanglement measures [9]. On the other hand, very little information is needed to settle the question of separability, and complete quantum tomography is certainly not necessary. For instance, the criterion $F > \frac{1}{2}$ can be relaxed to include only measurements of σ_x and σ_z, becoming $|\langle\sigma_x \otimes \sigma_x\rangle + \langle\sigma_z \otimes \sigma_z\rangle| > 1$ at the expense of requiring slightly higher correlations; this simplified measurement scheme corresponds to the most common description of the quantum eraser experiment.

VI. CONCLUSION AND OUTLOOK

We have described conceptually simple quantum eraser experiments based on free electrons and light that appear within reach of current technology, to both generate and verify electron-light entanglement. The above scheme allows a simple extension to generate entanglement between free electrons. Suppose two pairs of electron-photon entangled states $(|L, V\rangle + |R, H\rangle) \otimes (|L, V\rangle + |R, H\rangle)$ are generated. Then a Bell-state projection $\langle V, H| + \langle H, V|$ on the photon pair will result in path entangled electrons $|L, R\rangle + |R, L\rangle$, effectively performing entanglement swapping on the electron-photon pairs. The technique is very flexible and can be adapted to a wide range of scenarios involving different kinds of electron beams [26,74,75]. In general, quantum entanglement between any number of electrons $|L\rangle^{\otimes N} + |R\rangle^{\otimes N}$ can be established from N electron-photon pairs by projecting the photons onto the Greenberger-Horne-Zeilinger state $|V\rangle^{\otimes N} + |H\rangle^{\otimes N}$ [76]. Such states may be applied in TEMs to enhance the sensitivity to phase shifts due to the electrons experiencing the atomic potentials while passing through a sample. These phase shifts, investigated in the study of sample compositions and structures, are exceedingly small and the number of measurements at a single sample position is limited by radiation-induced irreversible damage. The sensitivity of the measurements could be improved by a factor of $N^{-1/2}$ when using N-electron entangled states M times [6] because the root-mean-square error in phase shift measurements will scale as $(\sqrt{M}N)^{-1}$, while for $M \times N$ uses of uncorrelated single electrons the error would scale as $(\sqrt{MN})^{-1}$ instead (see Appendix D for further details). Such entanglement-based improvements to sensitivities below the standard quantum limit $N^{-1/2}$ are also pursued in so-called quantum electron microscopes [45,47] and our work can provide an alternative specific route towards the realization of such an instrument. We note a recent publication also addressing electron-photon entanglement in electron microscopy [77].

ACKNOWLEDGMENTS

The authors would like to thank M. Sivis, O. Kfir, A. Feist, G. Arend, P. Haslinger, V. Di Giulio, and J. G. de Abajo for insightful discussions. This work was funded by the Deutsche Forschungsgemeinschaft (German Research Foundation) through Grant No. 432680300/SFB 1456 (Project No. C01) and the Gottfried Wilhelm Leibniz program, and the European Union's Horizon 2020 research and innovation program under Grant Agreement No. 101017720 (FET-Proactive EBEAM).

APPENDIX A: QUANTUM ERASER

This Appendix aims to provide a more detailed derivation of the electron intensity distributions described in Secs. II and III.

The intensity distribution for electrons on the screen behind the double slit can be calculated via

$$\begin{aligned}I(x) = \langle x|\rho|x\rangle &= |a|^2|\langle x|U|L\rangle|^2 + |b|^2|\langle x|U|R\rangle|^2\\&\quad + ab^*\langle x|U|L\rangle\langle R|U^\dagger|x\rangle + a^*b\langle x|U|R\rangle\langle L|U^\dagger|x\rangle,\end{aligned}$$

where $\langle x|\rho|x\rangle$ is the density matrix in the position representation and U is the propagator for the electrons from the slit plane with the left and right slits (denoted by $|L\rangle$ and $|R\rangle$, respectively) to any given point x in the detector plane. At short distances, U can be approximated by the Fresnel propagator [78], while in the far field, it reduces to the Fourier transform $\mathcal{F}$. Associating wave functions in the slit plane with the coordinate x', we can evaluate the expression above explicitly,

$$\begin{aligned}I(x) &= |a|^2|\mathcal{F}(\langle x'|L\rangle)|^2 + |b|^2|\mathcal{F}(\langle x'|R\rangle)|^2\\&\quad + ab^*e^{-i\phi(x)}\mathcal{F}(\langle x'|L\rangle)\mathcal{F}^*(\langle x'|R\rangle)\\&\quad + a^*be^{i\phi(x)}\mathcal{F}(\langle x'|R\rangle)\mathcal{F}^*(\langle x'|L\rangle)\\&= I_0(x) + I_0(x)\cos[\phi(x)],\end{aligned}$$

where $\phi(x)$ is the phase difference accumulated between electrons from the two slits to a point x on the detector and $I_0(x)$ describes the single-slit diffraction pattern, assuming evenly illuminated ($a = b$) identical slits. To simplify notation, we use a shorthand for the Fourier transform acting on wave functions, using expressions such as $\mathcal{F}(\langle x'\rangle L)$ in place of the more cumbersome $\mathcal{F}(\langle x'\rangle L)(x)$ when it is clear what arguments the transformed function must take. Similarly, we write $\mathcal{F}^*$ for the complex conjugate of the inverse Fourier transform.

Now suppose that an electron passing through the left slit generates a single photon with horizontal polarization $|H\rangle$, while an electron passing through the right slit generates a photon with vertical polarization $|V\rangle$. Then the joint quantum state of the electron-photon pair could be written as

$$\begin{aligned}\rho &= |a|^2|L, H\rangle\langle L, H| + |b|^2|R, V\rangle\langle R, V|\\&\quad + ab^*|L, H\rangle\langle R, V| + a^*b|R, V\rangle\langle L, H|,\end{aligned}$$

resulting in an electron intensity distribution on the camera given by

$$\begin{aligned}I(x) &= \langle x|\mathrm{Tr}_{\mathrm{ph}}(U\rho U^\dagger)|x\rangle\\&= |a|^2|\mathcal{F}(\langle x'|L\rangle)|^2 + |b|^2|\mathcal{F}(\langle x'|R\rangle)|^2\\&= I_0(x).\end{aligned}$$

Here $\mathrm{Tr}_{\mathrm{ph}}(\rho)$ is the partial trace over the photonic degrees of freedom and the last line again assumes even illumination of identical double slits. Clearly, the entanglement induced by the generation of marker photons removes the interference pattern, as the photons now carry information about which path the electron has taken.

Collecting the generated marker photons and passing them through a half waveplate [cf. Fig. 1(a)] transforms the polarization states in the following manner: $|H\rangle \rightarrow (|H\rangle + |V\rangle)/\sqrt{2}$ and $|V\rangle \rightarrow (|H\rangle - |V\rangle)/\sqrt{2}$. By inserting a polarizing beam splitter that separates the orthogonal polarizations $|H\rangle$ and $|V\rangle$ in the beam path, the quantum state of the electron conditioned on the detection of a photon with polarization $|H\rangle$ becomes

$$\begin{aligned}\tilde{\rho} &= \frac{(\mathbb{1}\otimes|H\rangle\langle H|)\rho(\mathbb{1}\otimes|H\rangle\langle H|)}{\mathrm{Tr}\rho(\mathbb{1}\otimes|H\rangle\langle H|)}\\ &= |a|^2U|L,H\rangle\langle L,H|U^\dagger + |b|^2U|R,H\rangle\langle R,H|U^\dagger\\ &\quad + ab^*U|L,H\rangle\langle R,H|U^\dagger + a^*bU|R,H\rangle\langle L,H|U^\dagger,\end{aligned}$$

where $\mathbb{1}$ denotes the identity operator. This results in the intensity distribution

$$\begin{aligned}I_e(x) &= |a|^2|\mathcal{F}(\langle x'|L\rangle)|^2 + |b|^2|\mathcal{F}(\langle x'|R\rangle)|^2\\ &\quad + ab^*e^{-i\phi(x)}\mathcal{F}(\langle x'|L\rangle)\mathcal{F}^*(\langle x'|R\rangle)\\ &\quad + a^*be^{i\phi(x)}\mathcal{F}(\langle x'|R\rangle)\mathcal{F}^*(\langle x'|L\rangle)\\ &= I_0(x) + I_0(x)\cos[\phi(x)],\end{aligned}$$

where the interference fringes are recovered. Analogously, postselecting photons of polarization $|V\rangle$ behind the half waveplate results in an interference pattern with inverted minima and maxima due to a sign change in the last two terms.

More generally, if the marker photons are not perfectly orthogonal, i.e., the postinteraction state reads $|\psi\rangle = a|L,H\rangle + b|R\rangle\otimes(h|H\rangle + v|V\rangle)$, both the unconditioned and the path-information-erased conditioned intensity distributions I_u and I_c, respectively, are modified:

$$\begin{aligned}I_u(x) &= |a|^2|\mathcal{F}(\langle x'|L\rangle)|^2 + |b|^2|\mathcal{F}(\langle x'|R\rangle)|^2\\ &\quad + ab^*h^*e^{-i\phi(x)}\mathcal{F}(\langle x'|L\rangle)\mathcal{F}^*(\langle x'|R\rangle)\\ &\quad + a^*bhe^{i\phi(x)}\mathcal{F}(\langle x'|R\rangle)\mathcal{F}^*(\langle x'|L\rangle)\\ &= I_0(x) + \mathrm{Re}(h)I_0(x)\cos[\phi(x)]\end{aligned}$$

and

$$\begin{aligned}I_c(x) &= |a|^2|\mathcal{F}(\langle x'|L\rangle)|^2 + |b|^2(1 + h^*v + hv^*)|\mathcal{F}(\langle x'|R\rangle)|^2\\ &\quad + ab^*(h^* + v^*)e^{-i\phi(x)}\mathcal{F}(\langle x'|L\rangle)\mathcal{F}^*(\langle x'|R\rangle)\\ &\quad + a^*b(h + v)e^{i\phi(x)}\mathcal{F}(\langle x'|R\rangle)\mathcal{F}^*(\langle x'|L\rangle)\\ &= [1 + \mathrm{Re}(h^*v)]I_0(x) + \mathrm{Re}(h + v)I_0(x)\cos[\phi(x)].\end{aligned}$$

The unconditioned intensity distribution $I_u(x)$ exhibits oscillations for $h \neq 0$ as the marker photons are no longer perfectly distinguishable. At the same time, the impact on the conditioned intensity distribution $I_c(x)$ reconstructed from the electron-photon coincidences after manipulation is less pronounced. Both the unconditioned and the recovered conditioned intensity patterns can be characterized by a corresponding visibility V_f of the interference fringes, shown in Fig. 1(d).

The description of the quantum eraser process can be further modified to account for limited spatial coherence by replacing the electron state below the slit with the mixed state,

$$\begin{aligned}\rho &= \gamma|\psi\rangle\langle\psi| + (1-\gamma)[|a|^2|L,H\rangle\langle L,H|\\ &\quad + |b|^2|R\rangle\otimes(h|H\rangle + v|V\rangle)(h^*\langle H| + v^*\langle V|)\otimes\langle R|],\end{aligned}$$

where γ is linked to the degree of transverse coherence. In this mixed-state case the concurrence C is defined as $C(\rho) = \max(0, \lambda_1 - \lambda_2 - \lambda_3 - \lambda_4)$, where the λ_i denote the eigenvalues, in decreasing order, of $R = \sqrt{\sqrt{\rho}\tilde{\rho}\sqrt{\rho}}$, with $\tilde{\rho} = (\sigma_y^e\otimes\sigma_y^{\mathrm{ph}})\rho^*(\sigma_y^e\otimes\sigma_y^{\mathrm{ph}})$ and the Pauli matrix σ_y. Figure 1(e) presents the relation between the concurrence and the visibility of the recovered conditioned intensity pattern for this simple model.

APPENDIX B: EXPERIMENTAL FEASIBILITY

This Appendix aims to illustrate the feasibility of our proposed quantum eraser experiment by estimating the required values for the parameters of polarization overlap $|h|^2$ and coherence γ and comparing them to the existing literature.

The coherence γ of the electrons in the double-slit setup is determined by the slit separation relative to the transverse coherence length $l_{\mathrm{coh,tr}}$ of the beam [79],

$$l_{\mathrm{coh,tr}} = \frac{\hbar}{m_e c}\frac{\sigma_x}{\varepsilon_{n,\mathrm{rms}}},$$

which is dominated by the emittance $\varepsilon_{n,\mathrm{rms}}$ of the electron source and the electron-beam spread σ_x. Thus, the coherence γ can be increased by appropriate widening and adjusting of the beam at the cost of reducing the electron current density on the two slits [80,81]. Because of their higher brightness [82], cold-field emission electron sources are beneficial for applications like electron holography that rely on high coherence [61–63,83]. However, Schottky-field emission sources in conjunction with grating plates have also demonstrated electron interference with the fringe visibility and thus the coherence reaching values as high as $\gamma \approx 0.70$ [64].

The electron-driven generation of linearly polarized light, on the other hand, has been observed for transition radiation in polarization-resolved cathodoluminescence [59,60]. We therefore conservatively estimate a possible polarization overlap $|h|^2 < 0.25$ for transition radiation generated from two distinctly shaped separated emission regions. Similarly, such a small state overlap should be achievable for two spatially separated emission regions coupled to distinct photon pathways.

Based on these considerations, we assume $\gamma = 0.65$ and $|h|^2 = 0.25$ and estimate the fringe visibilities and entanglement measures using our simple model. We find the fringe visibility in the unconditioned and conditioned recovered intensity patterns to be approximately 0.33 and approximately 0.63, respectively. Both the concurrence ($C \approx 0.56$) and the entanglement criterion derived from the entanglement witness [cf. Eq. (C1)] indicate entanglement for these parameters. Comparing the unconditioned and conditioned interference fringe visibilities, the ratio of the conditioned to the unconditioned is approximately 2, in line with the intuition that interference should be visible only in the path-erased conditioned case for electron-photon entanglement.

The almost one-to-one correspondence between the conditioned fringe visibility V_f and the concurrence C at small polarization overlaps is illustrated in Fig. 1(e) and a similar behavior is found for the entanglement criterion derived from the entanglement witness [cf. Fig. 3(b)]. We identify a range of parameters given by $|h|^2 \leqslant 0.25$ and $\gamma > 0.35$ for which the difference in fringe visibility is significant and both the entanglement criterion according to Eq. (C1) and the concurrence are sufficiently high ($C > 0.3$). These criteria are illustrated in Figs. 3(a) and 3(b), respectively, as a function of the model parameters $|h|^2$ and γ. The blacked dashed lines indicate the range of parameters with low polarization overlap for which both entanglement criteria are fulfilled. At larger electron coherences γ, the range of overlap $|h|^2$ for which entanglement can be detected increases, albeit leading to smaller differences between unconditioned and conditioned visibility.

It is worth noting that both the polarization overlap $|h|^2$ and the coherence γ can, in principle, be quantified in measurements independent of those directly required for the quantum eraser. The former can be determined by analyzing the polarization states generated at the two slits by a focused electron probe in STEM mode, while the latter can be estimated from the visibility of interference fringes in the diffraction of elastic electrons, i.e., filtering for electrons that did not lose energy. Consequently, with a precharacterization ensuring sufficiently small polarization overlap and large coherence, the comparison of unconditioned and conditioned fringe visibilities could provide sufficient evidence for entanglement.

APPENDIX C: QUANTUM STATE TOMOGRAPHY

This Appendix aims to provide background information for Sec. V.

The electron-photon quantum state in the proposed experimental scenario is equivalent to a two-qubit state and can be represented in the form

$$\rho = a\mathbb{1}\otimes\mathbb{1} + \sum_{i=x,y,z}\left(b_i\sigma_i^e\otimes\mathbb{1} + c_i\mathbb{1}\otimes\sigma_i^{\mathrm{ph}}\right) + \sum_{i,j=x,y,z} d_{ij}\sigma_i^e\otimes\sigma_j^{\mathrm{ph}},$$

with σ_k for $k = x, y, z$ as the three Pauli matrices as usual and superscripts e and ph to emphasize whether we are referring to the electron or photon. We take as eigenstates of σ_z the basis $\{|L\rangle, |R\rangle\}$ for the electron and $\{|H\rangle, |V\rangle\}$ for the photon. The coefficients are determined by local measurements of the corresponding observables

$$\begin{aligned} b_i &= \mathrm{Tr}[(\sigma_i\otimes\mathbb{1})\rho],\\ c_i &= \mathrm{Tr}[(\mathbb{1}\otimes\sigma_i)\rho],\\ d_{ij} &= \mathrm{Tr}[(\sigma_i\otimes\sigma_j)\rho],\end{aligned}$$

and with a fixed by normalization. The density matrix of the two-qubit system could be completely determined as long as one could implement measurements in all three bases independently for the electron and for the photon.

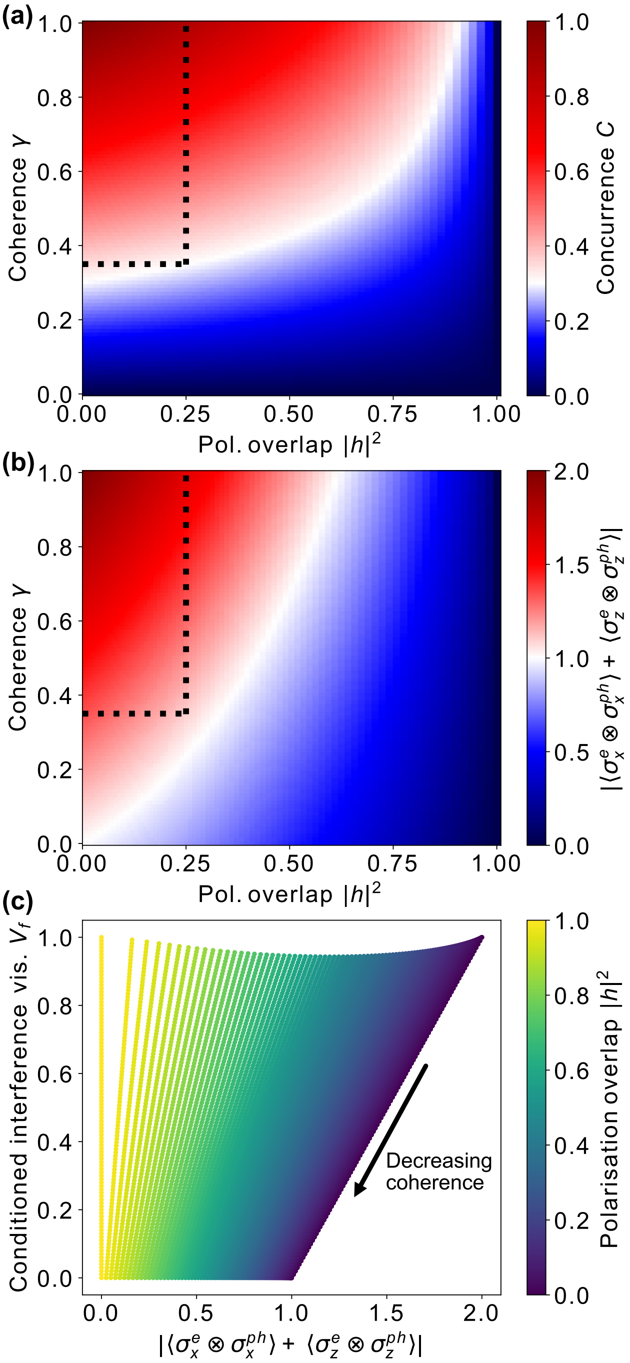

FIG. 3. Estimation of parameters from entanglement criteria. (a) Concurrence C evaluated over a range of polarization overlaps $|h|^2$ and input coherences γ. The color scale is chosen to highlight the region with $C \geqslant 0.3$. (b) Expectation values for the entanglement criterion derived from the entanglement witness as defined in Eq. (C1) over polarization overlap and coherence. The color scale is chosen such that values above 1, indicating entanglement, are shown in red. (c) Interference fringe visibility V_f in the recovered conditioned distribution versus the expectation value in the entanglement criterion of Eq. (C1) for different polarization overlap $|h|^2$ (color coded) and input coherences.

On the photon side, measurements of the three Pauli observables correspond to projections onto the different polarization states, i.e., horizontal or vertical (σ_z), diagonal

(σ_x), and left and right-handed circular polarizations (σ_y), and these can be implemented in the usual way by using half waveplates, quarter waveplates, polarizing beam splitters, and avalanche photon detection. On the electron side, the situation is more complicated but, nevertheless, measurements in all three bases can be implemented. A real-space image of the two slits obtained in the conventional imaging mode of the microscope tells us which slit the electron goes through, thus realizing a measurement of σ_z. Diffractograms obtained in the diffraction mode correspond to interference between the two beams with some relative phase shift $\phi(x)$, with x denoting the position on the screen, so that the detection of an electron at a position x on the screen corresponds to the projection operator $\langle L| + e^{i\phi(x)}\langle R|$. Therefore, measurements in the diffraction plane allow us to measure σ_x and σ_y. Complete knowledge of the density matrix can then be used to evaluate entanglement measures such as the concurrence C or the negativity [9].

Alternatively, the separability of the state could also be ascertained through fewer measurements by employing entanglement witnesses [9,10]. The joint electron-photon quantum state is ideally represented by the maximally entangled state $|\psi\rangle = (|L, H\rangle + |R, V\rangle)/\sqrt{2}$; thus we should consider the fidelity between this state and an experimentally generated state ρ,

$$\begin{aligned} F &= \langle\psi|\rho|\psi\rangle \\ &= \tfrac{1}{4}\mathrm{Tr}\big[\rho\big(\mathbb{1} + \sigma_x^e \otimes \sigma_x^{\mathrm{ph}} - \sigma_y^e \otimes \sigma_y^{\mathrm{ph}} + \sigma_z^e \otimes \sigma_z^{\mathrm{ph}}\big)\big], \end{aligned}$$

where the expression in the second line follows from the expansion of the state $|\psi\rangle\langle\psi|$ in the Pauli operators. Expectation values of outer products of Pauli operators can be measured as described above and a value of $F > \frac{1}{2}$ is sufficient for entanglement given the entanglement witness $\mathcal{W} = \frac{1}{2} - |\psi\rangle\langle\psi|$ [10]. The expectation value of $\mathcal{W}$ can be expressed as $\langle\mathcal{W}\rangle = \frac{1}{2} - F(\rho, |\psi\rangle\langle\psi|)$, so $\langle\mathcal{W}\rangle < 0$ is equivalent to $F > \frac{1}{2}$. By applying the triangle inequality, the inseparability criterion above could be further reduced to

$$\big|\big\langle\sigma_x^e \otimes \sigma_x^{\mathrm{ph}}\big\rangle + \big\langle\sigma_z^e \otimes \sigma_z^{\mathrm{ph}}\big\rangle\big| > 1, \tag{C1}$$

which describes the standard quantum eraser scenario with measurements in two linearly polarized bases.

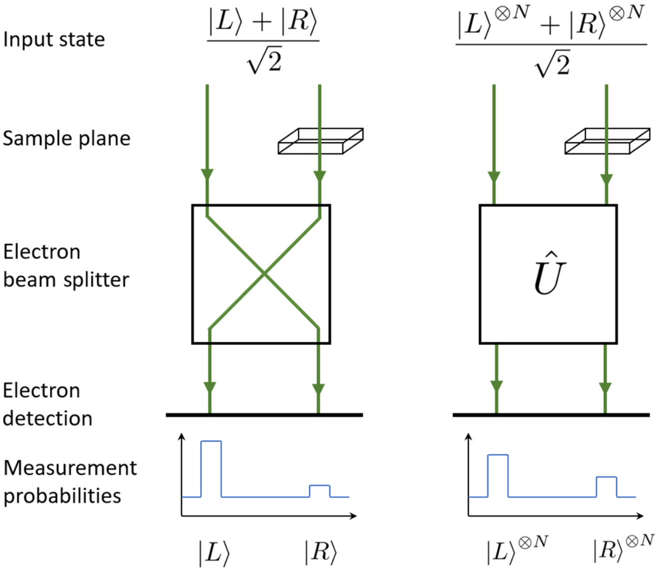

FIG. 4. Quantum metrology with entangled electrons. Electrons are labeled by two states $|L\rangle$ and $|R\rangle$ that propagate along two different paths (green lines). Following interaction with the sample, the two beams are brought into interference and measured on an electron camera; the population of electrons at each output port of the beam splitter is directly related to the phase shift due to the sample.

APPENDIX D: QUANTUM METROLOGY WITH ENTANGLED ELECTRONS

This Appendix aims to describe how the problem of phase estimation, most often considered in the context of optical and atomic systems, transfers to free electrons and how the use of quantum entanglement enables more precise measurements.

In the case of uncorrelated electrons (Fig. 4), each electron is initialized in the state $(|L\rangle + |R\rangle)/\sqrt{2}$ by dividing an electron beam into two equal parts using an electron beam splitter, and the entire beam could be written as a tensor product of electrons $((|L\rangle + |R\rangle)/\sqrt{2})^{\otimes N}$. Only the $|R\rangle$ state is made to pass through the sample, so after the interaction the electrons are transformed into the state $(|L\rangle + e^{i\phi}|R\rangle)/\sqrt{2}$, where ϕ denotes the phase shift imparted on the electron by the sample. To obtain information about the phase shift, a second beam splitter should be used to undo the superposition, after which the probabilities of the electron emerging from either port are measured. These probabilities are

$$\begin{aligned} P_L &= \frac{\langle L| + \langle R|}{\sqrt{2}}\,\frac{|L\rangle + e^{i\phi}|R\rangle}{\sqrt{2}} = \frac{1}{4}|1 + e^{i\phi}|^2, \\ P_R &= \frac{\langle L| - \langle R|}{\sqrt{2}}\,\frac{|L\rangle + e^{i\phi}|R\rangle}{\sqrt{2}} = \frac{1}{4}|1 - e^{i\phi}|^2. \end{aligned}$$

For simplicity, let us assume that the phase shift is small $\phi \ll 1$, which is the case in electron microscopy. Then this phase shift can be related to the transition probability into the orthogonal state $P_R = \frac{1}{4}|1 - e^{i\phi}|^2 \approx \phi^2/4$, and its error is derived through the usual methods of error propagation:

$$d\phi = \frac{2}{\phi}dP_R.$$

Invoking the central-limit theorem, the error in determining the probability P_R through repeated sampling of the probability distribution $\{P_L, P_R\}$ scales as $1/\sqrt{N}$, and therefore the error in determining the phase shift ϕ also scales as $1/\sqrt{N}$.

The situation for entangled states of electrons is very similar to what we have described above, but with the initial state replaced by entangled states of N electrons $(|L\rangle^{\otimes N} + |R\rangle^{\otimes N})/\sqrt{2}$, the electron beam splitter $\hat{U}$ generalized to operate on the logical basis $\{|L\rangle^{\otimes N}, |R\rangle^{\otimes N}\}$, and the measurements now projecting onto N electron states $|L\rangle^{\otimes N}$ and $|R\rangle^{\otimes N}$. Analogous to the case of uncorrelated electrons, the purpose of the measurement is to determine the overlap between the phase-shifted electrons and the states $(|L\rangle^{\otimes N} \pm |R\rangle^{\otimes})/\sqrt{2}$, and the associated probabilities are

$$\begin{aligned} P_L &= |1 + e^{iN\phi}|/4, \\ P_R &= |1 - e^{iN\phi}|/4. \end{aligned}$$

For small phase shifts $P_R \approx N^2\phi^2/4$, so the error in the phase shift scales as

$$d\phi = \frac{2}{N^2\phi} dP_R.$$

Because the probability distribution $\{P_L, P_R\}$ has variance $(N^2\phi^2/4)(1 - N^2\phi^2/4) \approx N^2\phi^2/4$, the central-limit theorem implies that dP_R scales as $N/\sqrt{M}$, where M is the number of uses of such entangled states of N electrons. The error in determining the phase shift therefore scales as $1/N\sqrt{M}$, which is a factor of $1/\sqrt{N}$ lower compared to using $M \times N$ uncorrelated electrons.

Finally, we remark that everything we have said applies equally to any value of the phase shift ϕ provided the formulas above are adjusted accordingly and mostly in a trivial manner.

---

[1] M. A. Nielsen and I. L. Chuang, *Quantum Computation and Quantum Information*, 2nd ed. (Cambridge University Press, New York, 2010).

[2] T. D. Ladd, F. Jelezko, R. Laflamme, and Y. Nakamura, Nature (London) **464**, 45 (2010).

[3] N. Gisin, G. Ribordy, W. Tittel, and H. Zbinden, Rev. Mod. Phys. **74**, 145 (2002).

[4] K. Azuma, S. E. Economou, D. Elkouss, P. Hilaire, L. Jiang, H.-K. Lo, and I. Tzitrin, Rev. Mod. Phys. **95**, 045006 (2023).

[5] S. Wehner, D. Elkouss, and R. Hanson, Science **362**, eaam9288 (2018).

[6] V. Giovannetti, S. Lloyd, and L. Maccone, Nat. Photon. **5**, 222 (2011).

[7] C. L. Degen, F. Reinhard, and P. Cappellaro, Rev. Mod. Phys. **89**, 035002 (2017).

[8] X.-s. Ma, J. Kofler, and A. Zeilinger, Rev. Mod. Phys. **88**, 015005 (2016).

[9] R. Horodecki, P. Horodecki, M. Horodecki, and K. Horodecki, Rev. Mod. Phys. **81**, 865 (2009).

[10] O. Gühne and G. Tóth, Phys. Rep. **474**, 1 (2009).

[11] J. F. Clauser, M. A. Horne, A. Shimony, and R. A. Holt, Phys. Rev. Lett. **23**, 880 (1969).

[12] A. Aspect, P. Grangier, and G. Roger, Phys. Rev. Lett. **49**, 91 (1982).

[13] S. Storz, J. Schär, A. Kulikov, P. Magnard, P. Kurpiers, J. Lütolf, T. Walter, A. Copetudo, K. Reuer, A. Akin, J.-C. Besse, M. Gabureac, G. J. Norris, A. Rosario, F. Martin, J. Martinez, W. Amaya, M. W. Mitchell, C. Abellan, J.-D. Bancal *et al.*, Nature (London) **617**, 265 (2023).

[14] J. G. Rarity and P. R. Tapster, Phys. Rev. Lett. **64**, 2495 (1990).

[15] T. J. Herzog, P. G. Kwiat, H. Weinfurter, and A. Zeilinger, Phys. Rev. Lett. **75**, 3034 (1995).

[16] S. P. Walborn, M. O. T. Cunha, S. Pádua, and C. H. Monken, Phys. Rev. A **65**, 033818 (2002).

[17] Y.-H. Kim, R. Yu, S. P. Kulik, Y. Shih, and M. O. Scully, Phys. Rev. Lett. **84**, 1 (2000).

[18] F. Kaiser, T. Coudreau, P. Milman, D. B. Ostrowsky, and S. Tanzilli, Science **338**, 637 (2012).

[19] S. Dürr, T. Nonn, and G. Rempe, Nature (London) **395**, 33 (1998).

[20] E. Weisz, H. K. Choi, I. Sivan, M. Heiblum, Y. Gefen, D. Mahalu, and V. Umansky, Science **344**, 1363 (2014).

[21] A. Bienfait, Y. P. Zhong, H.-S. Chang, M.-H. Chou, C. R. Conner, É. Dumur, J. Grebel, G. A. Peairs, R. G. Povey, K. J. Satzinger, and A. N. Cleland, Phys. Rev. X **10**, 021055 (2020).

[22] K. M. Yip, N. Fischer, E. Paknia, A. Chari, and H. Stark, Nature (London) **587**, 157 (2020).

[23] P. Baum, D.-S. Yang, and A. H. Zewail, Science **318**, 788 (2007).

[24] T. Danz, T. Domröse, and C. Ropers, Science **371**, 371 (2021).

[25] P. Schattschneider and S. Löffler, Ultramicroscopy **190**, 39 (2018).

[26] O. Kfir, Phys. Rev. Lett. **123**, 103602 (2019).

[27] Z. Zhao, X.-Q. Sun, and S. Fan, Phys. Rev. Lett. **126**, 233402 (2021).

[28] A. Konečná, F. Iyikanat, and F. J. García de Abajo, Sci. Adv. **8**, eabo7853 (2022).

[29] F. J. García de Abajo, Rev. Mod. Phys. **82**, 209 (2010).

[30] S. Meuret, L. H. G. Tizei, T. Cazimajou, R. Bourrellier, H. C. Chang, F. Treussart, and M. Kociak, Phys. Rev. Lett. **114**, 197401 (2015).

[31] M. Solà-Garcia, K. W. Mauser, M. Liebtrau, T. Coenen, S. Christiansen, S. Meuret, and A. Polman, ACS Photon. **8**, 916 (2021).

[32] M. Scheucher, T. Schachinger, T. Spielauer, M. Stöger-Pollach, and P. Haslinger, Ultramicroscopy **241**, 113594 (2022).

[33] S. Fiedler, S. Morozov, D. Komisar, E. A. Ekimov, L. F. Kulikova, V. A. Davydov, V. N. Agafonov, S. Kumar, C. Wolff, S. I. Bozhevolnyi, and N. A. Mortensen, Nanophotonics **12**, 2231 (2023).

[34] B. Barwick, D. J. Flannigan, and A. H. Zewail, Nature (London) **462**, 902 (2009).

[35] A. Feist, K. E. Echternkamp, J. Schauss, S. V. Yalunin, S. Schäfer, and C. Ropers, Nature (London) **521**, 200 (2015).

[36] L. Piazza, T. Lummen, E. Quiñonez, Y. Murooka, B. Reed, B. Barwick, and F. Carbone, Nat. Commun. **6**, 6407 (2015).

[37] D. Nabben, J. Kuttruff, L. Stolz, A. Ryabov, and P. Baum, Nature (London) **619**, 63 (2023).

[38] Y. Yang, J.-W. Henke, A. S. Raja, F. J. Kappert, G. Huang, G. Arend, Z. Qiu, A. Feist, R. N. Wang, A. Tusnin, A. Tikan, C. Ropers, and T. J. Kippenberg, Science **383**, 168 (2024).

[39] K. E. Priebe, C. Rathje, S. V. Yalunin, T. Hohage, A. Feist, S. Schäfer, and C. Ropers, Nat. Photon. **11**, 793 (2017).

[40] J. H. Gaida, H. Lourenço-Martins, M. Sivis, T. Rittmann, A. Feist, F. J. García de Abajo, and C. Ropers, Nat. Photon. **18**, 509 (2024).

[41] V. Di Giulio, M. Kociak, and F. J. G. de Abajo, Optica **6**, 1524 (2019).

[42] R. Dahan, A. Gorlach, U. Haeusler, A. Karnieli, O. Eyal, P. Yousefi, M. Segev, A. Arie, G. Eisenstein, P. Hommelhoff, and I. Kaminer, Science **373**, eabj7128 (2021).

[43] A. Feist, G. Huang, G. Arend, Y. Yang, J.-W. Henke, A. S. Raja, F. J. Kappert, R. N. Wang, H. Lourenço-Martins, Z. Qiu, J. Liu, O. Kfir, T. J. Kippenberg, and C. Ropers, Science **377**, 777 (2022).

[44] N. Varkentina, Y. Auad, S. Y. Woo, A. Zobelli, L. Bocher, J.-D. Blazit, X. Li, M. Tencé, K. Watanabe, T. Taniguchi, O. Stéphan, M. Kociak, and L. H. G. Tizei, Sci. Adv. **8**, eabq4947 (2022).

[45] P. Kruit, R. G. Hobbs, C.-S. Kim, Y. Yang, V. R. Manfrinato, J. Hammer, S. Thomas, P. Weber, B. Klopfer, C. Kohstall, T. Juffmann, M. A. Kasevich, P. Hommelhoff, and K. K. Berggren, Ultramicroscopy **164**, 31 (2016).

[46] A. E. Turner, C. W. Johnson, P. Kruit, and B. J. McMorran, Phys. Rev. Lett. **127**, 110401 (2021).

[47] S. A. Koppell, Y. Israel, A. J. Bowman, B. B. Klopfer, and M. A. Kasevich, Appl. Phys. Lett. **120**, 190502 (2022).

[48] E. Rotunno, S. Gargiulo, G. M. Vanacore, C. Mechel, A. H. Tavabi, R. E. Dunin-Borkowski, F. Carbone, I. Madan, S. Frabboni, T. Guner, E. Karimi, I. Kaminer, and V. Grillo, ACS Photon. **10**, 1708 (2023).

[49] X. Bendaña, A. Polman, and F. J. García de Abajo, Nano Lett. **11**, 5099 (2011).

[50] A. Ben Hayun, O. Reinhardt, J. Nemirovsky, A. Karnieli, N. Rivera, and I. Kaminer, Sci. Adv. **7**, eabe4270 (2021).

[51] R. Dahan, G. Baranes, A. Gorlach, R. Ruimy, N. Rivera, and I. Kaminer, Phys. Rev. X **13**, 031001 (2023).

[52] G. Arend, G. Huang, A. Feist, Y. Yang, J.-W. Henke, Z. Qiu, H. Jeng, A. S. Raja, R. Haindl, R. N. Wang, T. J. Kippenberg, and C. Ropers, Electrons herald non-classical light, arXiv:2409.11300.

[53] G. Baranes, R. Ruimy, A. Gorlach, and I. Kaminer, npj Quantum Inf. **8**, 32 (2022).

[54] C. Jönsson, Z. Phys. **161**, 454 (1961).

[55] R. Bach, D. Pope, S.-H. Liou, and H. Batelaan, New J. Phys. **15**, 033018 (2013).

[56] A. H. Tavabi, C. B. Boothroyd, E. Yücelen, S. Frabboni, G. C. Gazzadi, R. E. Dunin-Borkowski, and G. Pozzi, Sci. Rep. **9**, 10458 (2019).

[57] A. Zeilinger, Rev. Mod. Phys. **71**, S288 (1999).

[58] M. B. Plenio and S. Virmani, Quantum Inf. Comput. **7**, 1 (2007).

[59] T. Coenen and A. Polman, Opt. Express **20**, 18679 (2012).

[60] C. I. Osorio, T. Coenen, B. J. M. Brenny, A. Polman, and A. F. Koenderink, ACS Photon. **3**, 147 (2016).

[61] L. F. Allard and E. Völkl, in *Introduction to Electron Holography*, edited by E. Völkl, L. F. Allard, and D. C. Joy (Springer, Boston, 1999), pp. 57–86.

[62] A. Tonomura, Rev. Mod. Phys. **59**, 639 (1987).

[63] P. A. Midgley and R. E. Dunin-Borkowski, Nat. Mater. **8**, 271 (2009).

[64] T. R. Harvey, F. S. Yasin, J. J. Chess, J. S. Pierce, R. M. S. Dos Reis, V. B. Özdöl, P. Ercius, J. Ciston, W. Feng, N. A. Kotov, B. J. McMorran, and C. Ophus, Phys. Rev. Appl. **10**, 061001(R) (2018).

[65] T. R Harvey, J. S Pierce, A. K Agrawal, P. Ercius, M. Linck, and B. J. McMorran, New J. Phys. **16**, 093039 (2014).

[66] F. S. Yasin, T. R. Harvey, J. J. Chess, J. S. Pierce, and B. J. McMorran, J. Phys. D **51**, 205104 (2018).

[67] C. W. Johnson, A. E. Turner, and B. J. McMorran, Phys. Rev. Res. **3**, 043009 (2021).

[68] J. Christopher, M. Taleb, A. Maity, M. Hentschel, H. Giessen, and N. Talebi, Nanophotonics **9**, 4381 (2020).

[69] J.-K. So, K. F. MacDonald, and N. I. Zheludev, Appl. Phys. Lett. **104**, 201101 (2014).

[70] J.-K. So, F. J. García de Abajo, K. F. MacDonald, and N. I. Zheludev, ACS Photon. **2**, 1236 (2015).

[71] N. Müller, V. Hock, H. Koch, N. Bach, C. Rathje, and S. Schäfer, ACS Photon. **8**, 1569 (2021).

[72] E. Pomarico, I. Madan, G. Berruto, G. M. Vanacore, K. Wang, I. Kaminer, F. J. García de Abajo, and F. Carbone, ACS Photon. **5**, 759 (2018).

[73] J.-W. Henke, A. S. Raja, A. Feist, G. Huang, G. Arend, Y. Yang, F. J. Kappert, R. N. Wang, M. Möller, J. Pan, J. Liu, O. Kfir, C. Ropers, and T. J. Kippenberg, Nature (London) **600**, 653 (2021).

[74] R. Haindl, A. Feist, T. Domröse, M. Möller, J. H. Gaida, S. V. Yalunin, and C. Ropers, Nat. Phys. **19**, 1410 (2023).

[75] S. Meier, J. Heimerl, and P. Hommelhoff, Nat. Phys. **19**, 1402 (2023).

[76] D. M. Greenberger, M. A. Horne, and A. Zeilinger, in *Bell's Theorem, Quantum Theory and Conceptions of the Universe*, edited by M. Kafatos (Springer, Dordrecht, 1989), pp. 69–72.

[77] E. Kazakevich, H. Aharon, and O. Kfir, Phys. Rev. Res. **6**, 043033 (2024).

[78] A. Lubk, in *Advances in Imaging and Electron Physics*, edited by P. W. Hawkes (Elsevier, Amsterdam, 2018), Vol. 206, pp. 15–58.

[79] T. van Oudheusden, E. F. De Jong, S. B. Van Der Geer, W. P. E. M. Op 't Root, O. J. Luiten, and B. J. Siwick, J. Appl. Phys. **102**, 093501 (2007).

[80] D. B. Williams and C. B. Carter, in *Transmission Electron Microscopy: A Textbook for Materials Science*, edited by D. B. Williams and C. B. Carter (Springer, Boston, 2009), pp. 73–89.

[81] M. Lehmann, Ultramicroscopy **100**, 9 (2004).

[82] S. Mamishin, Y. Kubo, R. Cours, M. Monthioux, and F. Houdellier, Ultramicroscopy **182**, 303 (2017).

[83] P. A. Midgley, Micron **32**, 167 (2001).